

Photogrammetric Surface Analysis of Ablation Processes in High Enthalpy Air Plasma Flow

Stefan Loehle*, Tina Staebler[†],

*Institute of Space Systems, University of Stuttgart
Pfaffenwaldring 31, D-70569 Stuttgart, Germany*

Thomas Reimer[‡]

*German Aerospace Center, Institute of Structures and Design
Pfaffenwaldring 38-40, D-70569 Stuttgart, Germany*

Alessandro Cefalu[§]

*Institute of Photogrammetry, University of Stuttgart
Geschwister-Scholl-Str. 24d, D-70174 Stuttgart, Germany*

Results from in-situ analysis of ablative heat shield materials based on stereoscopic photogrammetry during plasma wind tunnel testing are presented. A carbon fiber preform material sample has been investigated in a high enthalpy air flow corresponding to a Hayabusa re-entry condition in 78 km altitude. The applied photogrammetry uses two digital single lens reflex (DSLR) cameras triggered at 3 fps to acquire images simultaneously from two different perspectives of the sample exposed to the high speed flow. The photogrammetric analysis resolves the surface with 25000 px/cm², approximately 400 dpi, allowing the in-situ analysis of the recession phenomena of ablators. Material inhomogeneities are identified during the ablation process and surface recession is derived with an accuracy of 21 μm.

*Research Scientist, Member AIAA

[†]Master student

[‡]Research Scientist, Member AIAA

[§]Research Scientist

The method is a useful tool for the investigation of temporally resolved volumetric ablation phenomena in low density carbon phenolic materials.

I. Introduction

Experimental investigation of the thermochemical performance of heat shield materials is usually conducted in so-called plasma wind tunnels.^{1,2} The state of the art diagnostic tools to judge the performance of the material during testing are based on the measurement of surface temperatures, in-depth temperatures using thermocouples and spectroscopic diagnostics in order to investigate the plasma layer in front of the tested materials.^{3,4} Classically, the performance of a char layer is described by the recession velocity assuming a steady state process at the surface. For measurement of the material's recession in ground testing the common approach is to compare the sample thickness before and after the test, however, this method does not give insight into transient processes that may be occurring. Experimental methods to assess the surface state during testing are missing. Furthermore, an in-situ surface structure analysis is not possible from this measurement.

In modern lightweight ablators, recession is generally occurring as a volumetric process in a layer of the material close to the surface, i.e. the ablation can occur in-depth.⁵ Low density ablators consist of a highly porous carbon preform. The pores are then filled with a phenolic resin. When the temperature increases, this virgin material decomposes and is destroyed. The main processes occurring are pyrolysis and ablation. Pyrolysis is the transformation of the phenolic resin into a gas to a low density carbon or a charred material. The material loses a major part of its mass through this process (on the order of 50%). The gases emerging during this process are injected into the boundary layer and this process is one important feature of how ablative heat shields function. The carbonaceous material is exposed to oxidation and nitridation with the gas, sublimation (at high temperatures) and eventually mechanical thermochemical surface erosion. The significance of nitridation for recession has been shown to be rather low.⁶ Sublimation, i.e. the phase change to gas of the carbon solid (char and fibers), becomes significant at high temperatures above 3000 K.^{5,7} However, mechanical erosion can be important depending on the surface state and surface layer porosity.

Therefore, ground testing methodologies need to be extended to enable a better understanding of these processes in ground test facilities. This paper presents a method for the in-situ analysis of the surface state during testing using stereoscopic photogrammetry.

In flight surface recession can only be determined using embedded sensors and sophisticated analysis tools. One of the recent developments is the recession sensor developed for the Mars Science Laboratory (MSL).^{8,9} In ground testing environments, however, the surface

can be observed using optical methods. Very simple approaches are based on the observation of laser spots on the surface, which change position when the material changes.¹⁰

The approach followed in the present work is the direct observation of the surface from different perspectives and the application of photogrammetric tools in order to determine the three-dimensional surface geometry. This technology has been successfully demonstrated by Schairer et al. for arcjet tests at NASA Ames using CCD video cameras.¹¹ This system acquired at a maximum frame rate of 16 Hz and a displacement uncertainty of 0.2 mm for a stagnation model and 0.3 mm for a panel model.

In this paper stereoscopic photogrammetry using two photo cameras, a combination of open source software tools, and commercial programs have been used to analyse simultaneously acquired photographs of the recessing surface. Modern photogrammetric software tools are based on a pixelwise analysis allowing a high geometrical resolution and a comparably high accuracy. Two digital single lens reflex (DSLR) cameras were adapted for plasma wind tunnel purposes using fixed focal length (300mm) lenses.

The method is tested using a carbon preform material (CALCARB). Its surface is assumed to be comparable to a low density carbon ablator surface. Within the present study, experimental results are presented from in-situ surface analysis of these material probe surfaces using photogrammetric analysis.

II. Experimental Setup

The material tests within this study have been conducted in the plasma wind tunnel PWK1 at IRS. A direct view onto the sample surface mounted in the probe inside the vacuum vessel for the photogrammetric system is provided through optical windows in the front lid. The probe is mounted on a moving platform inside the vacuum chamber.

The vacuum chamber (6 m in length and 2 m in diameter) is connected to the in-house vacuum pumping system. The generator RD5, a magnetoplasmadynamic arcjet,¹² is mounted in the front lid of the vessel. A current-regulated thyristor rectifier consisting of six identical units supplying 1 MW each, provides electric power. Samples and measurement equipment is mounted in corresponding water-cooled probes. The probes are moved axially inside the chamber to adjust the heat load and total pressure. To increase the number of measurements possible during each experiment, some probes have been manufactured with two heads so that two tests can be performed within one experiment by rotating the probe. The present investigation has been conducted with a probe that is usually used for material investigation of ablative test materials.^{7,13} The sample used is a carbon preform of type CALCARB with a probe diameter of 40 mm. This material has also been considered suitable in other facilities for fundamental ablation testing.¹⁴ Fig. 1 shows a photo of the probe as mounted in the

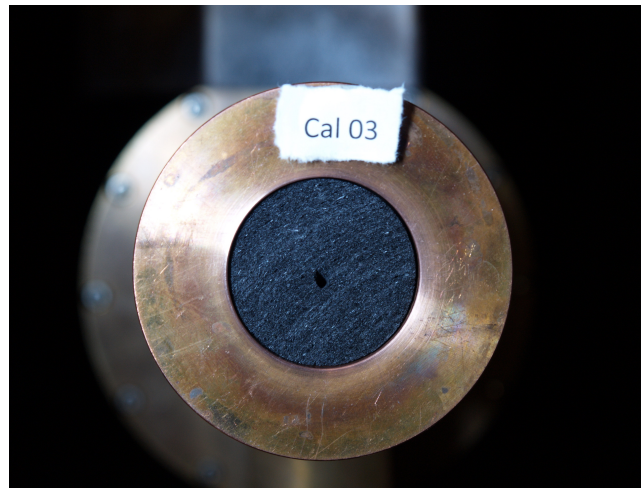


Figure 1: Material probe holder with mounted CALCARB probe.

sample holder. Originally, this probe setup was designed for testing samples equipped with thermocouples hier wÄr noch eine Referenz nett, aber die hab ich noch nicht gefunden. The outer, water-cooled copper ring allows the integration of thermocouples in the sample which are mounted in parallel to the surface, i.e. along the isotherm of the heated sample. With this setup, a more accurate temperature measurement has been tried.

A flow condition has been chosen which was developed for ground test analysis of the observed Hayabusa re-entry in 2010.^{15,16} This flow condition is also part of a research project funded by the European Space Agency (ESA) under the management of the Ecole Federale Polytechnique de Lausanne (EPFL).¹⁷ The material tests performed within this study were part of this ESA project.

The parameters of the chosen flow condition are summarized in Tab. 1. Heat flux and total pressure were measured in separate tests using the same probe geometry. Heat flux is derived from a calorimetric cold wall heat flux measurement on a pre-oxidized copper surface. A copper insert of the size of a material sample is integrated in the sample holder as seen in Fig. 1. This copper sample is cooled with a separate cooling circuit. By measuring the water cooling flow rate and the temperature difference between water inlet and outlet, the heat flux at the surface is determined. The mass-specific enthalpy is calculated with the approximation of Zoby from the one-dimensional stagnation point heat transfer equations developed by Fay and Riddell.^{18,19}

There are only small optical windows to observe the plasma flow and the probe. Fig. 2 shows a photograph and a schematic of the setup using two cameras. The best solution for photogrammetry is to use the two angled windows in the front lid of the vacuum chamber. Here, possible reflectivity issues are minimised and a comparably long path along the axial direction of the wind tunnel can be observed. The front lid has to be opened for sample

Table 1: Plasma wind tunnel condition for the condition corresponding to Hayabusa at 78.8 km

Parameter	Value
mass flow \dot{m}	18,0 $\frac{g}{s}$
ambient pressure p_∞	16,6 hPa
total pressure p_{tot}	24,3 hPa
arc current I	1220 A
arc voltage U	133 V
electric power P	162 kW
probe position	$x = 270 \text{ mm}, y = 0 \text{ mm}$
heat flux \dot{Q}	4100 $\frac{kW}{m^2}$
mass-specific enthalpy h	68,43 $\frac{MJ}{kg}$

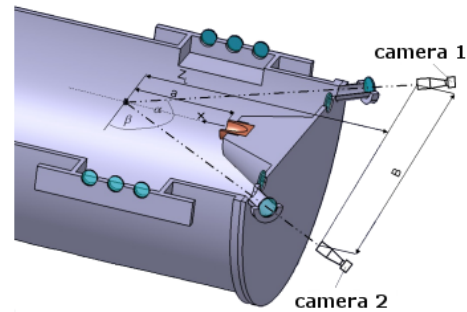
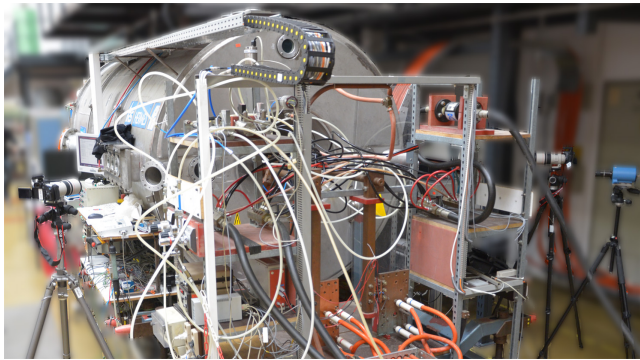


Figure 2: Plasma wind tunnel PWK1 (left) and geometrical setup for the photogrammetry (right).²⁰

installation, therefore, the cameras were mounted on separate tripods with sufficient distance to the facility. This has the further advantage that vibrations of the vacuum chamber during vacuum pumping startup do not affect the camera setup. A possible influence of the windows with respect to the photogrammetric measurements has been analysed during the previous work.²¹ In this configuration the angle between the imaging axis of the two cameras was between 95° and 100°. Depending on other instruments used in the experiment, the distance between probe and camera varies between 2.8 m and 4.0 m. A nearer position is preferable, but is restricted by the space required to open the front lid of the vacuum vessel.

The images are acquired using two CANON EOS 60D digital single lens reflex (DSLR) cameras. Two prime lenses with 300 mm focal length (CANON EF 300mm 1/4L IS USM) were used with the cameras. Table 2 lists the parameters of the camera setup. The cameras are triggered simultaneously within <100 ms of each other using a radio controlled trigger. For the present analysis, a frame rate of three images per second (fps) has been achieved.

The high luminosity of the probe required the use of a neutral density filter with an optical density of 1.2. This filter transmits only 6.3% of the incident light. A further important pa-

Table 2: Camera setup.

camera	Canon EOS 60 D
pixel resolution	5184 x 3456 px ²
chip size	22.3 x 14.9 mm ²
pixel size	4.3 μ m
aperture	25
ISO	100
exposure	1/4000 s
focal length	300 mm
colour depth	24 bit
neutral density filter	ND1.2
frame rate	3 fps
image format	jpeg

parameter of the measurements presented here is the surface temperature. Surface temperature has been measured using an LP3 linear pyrometer from KE TECHNOLOGIE GMBH. The pyrometer uses a Silicon based detector calibrated against the ITS-90 standard. Measured temperatures have an uncertainty of $< 2\%$. The measurement wavelength is 950 nm and the system focuses on a single spot with a diameter of ≈ 5 mm. The temperature is corrected for window transmission (measured SUPRASIL window transmission $\tau_{Window} = 0.92$) and surface emissivity (carbon value for emissivity assumed $\epsilon = 0.85$).

III. Theory

The general term *Photogrammetry* is the estimative method to determine the position of a point in space using two or more (two-dimensional) images of the scene under different view angles. *Stereophotogrammetry*, as used in this study, is understood as the calculation of the three-dimensional coordinates of points of a structure using only two views under two different view angles. As described before, two DSLR cameras have been used through two windows in the front lid of the plasma wind tunnel in order to observe the probe surface from two perspectives.

Three steps are required to analyse the images using three different software packages:

1. **Calibration:** Measurement of the position and orientation of the system. This is done with the software AGISOFT PHOTOSCAN. The output is a set of calibration parameters.
2. **Measurement:** The calibration parameters are applied to analyse measured image

pairs. This analysis is done using the software SURE. The output is a point cloud.

3. **Recession and Surface analysis:** The point clouds are loaded into the software CLOUDCOMPARE.

The first analysis step is conducted with AGISOFT PHOTOSCAN, a commercial software.²² The software is used to calculate the inner and outer orientations of the camera setup by using a separate set of images dedicated to the calibration.

This calibration was conducted with a generic three dimensionally structured image (see Fig. 3).



Figure 3: Structured calibration plate.

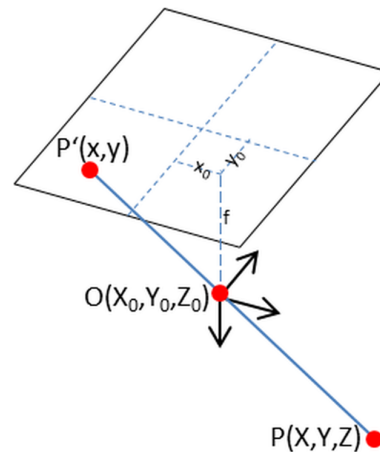


Figure 4: Photogrammetric nomenclature: Angles of rotation and the reference coordinate system are not shown for better visualization.

Using a structured surface with varying rectangles is best for a high calibration accuracy. The scale on the calibration plate is used for metric scaling. The calibration procedure is as follows: The cameras are set up at the wind tunnel and focused to the probe position. Then the calibration plate is mounted at this (the probe's) position. The calibration images are captured by rotating and tilting the plate following a photogrammetric standard calibration scheme.²³ These images are required to calculate the cameras' positions with respect to each other and the camera's sensor imaging geometries. These are called the outer and inner orientation, respectively.

The calibration images are loaded in PHOTOSCAN and assigned to the camera it was taken by (left image - left camera, right image - right camera). Image data (e.g. focus length) is automatically obtained from the image's exif data. If the calibration plate does not fully cover each image, masks are added or images are removed. First, PHOTOSCAN calculates approximated values for all unknowns (see Tab. 3) using a Structure-from-Motion approach. Here, point features in the images are automatically detected and described. The descriptors

Observed	
$P'(x, y)$	Image coordinates of a measured point
Unknown Inner Orientation	
f	focal length
$\Delta x, \Delta y$	Principal point (intersection of image plain and optical main axis)
Unknown Outer Orientation	
R	Rotation matrix (3 camera orientation angles), $r_{i,j} \rightarrow$ single entries
$O(X_0, Y_0, Z_0)$	Translation vector (camera position)
Unknown 3D-Points	
$P(X, Y, Z)$	Point coordinates in a reference system

Table 3: Photogrammetric parameters

are used to find correspondences between images, therefore a sufficiently textured calibration plate is required. In a second step, the results are refined by bundle adjustment. It utilizes the so called collinearity equations (Eqs. (1) and (2)), i.e. the mathematical description of the central perspective relation between a point P in 3D-space and its 2D-projection onto the camera’s image plane P' (see Fig. 4).

$$x = x_0 + f \frac{r_{11}(X - X_0) + r_{21}(Y - Y_0) + r_{31}(Z - Z_0)}{r_{13}(x - X_0) + r_{23}(Y - Y_0) + r_{33}(Z - Z_0)} + \Delta x \quad (1)$$

$$y = y_0 + f \frac{r_{12}(X - X_0) + r_{22}(Y - Y_0) + r_{32}(Z - Z_0)}{r_{13}(x - X_0) + r_{23}(Y - Y_0) + r_{33}(Z - Z_0)} + \Delta y \quad (2)$$

Within the adjustment, the model is further extended through additional lens distortion polynomials.

As mentioned, the results of this calibration is the calculation of the inner orientation of the cameras, i.e. the chip orientation, and the outer orientation, i.e. the position of the cameras with respect to each other. Fig. 5 shows the three-dimensional point map of the calibration plate. In this representation, the setup is virtually inverted: the image is fixed in space and the camera poitions are turned and tilted. The camera positions with respect to each other, however, are fix. Every square in Fig. 5 is a different camera position. The acquisition, however, was made by a steady camera and a tilted and rotated calibration plate. Since the distance between camera and calibration plate was not changed during calibration, the square images in Fig. 5 are aligned approximately on a half sphere.

A scale has been added in PHOTOSCAN using *markers* which are automatically assigned to the three dimensional model. Finally, one single stereo image pair with high accuracy

and good contrast is selected and its camera orientation is exported to a project file. As the orientation of the cameras relative to each other is constant during calibration and testing, the orientation can be used for all image pairs taken during the wind tunnel test.

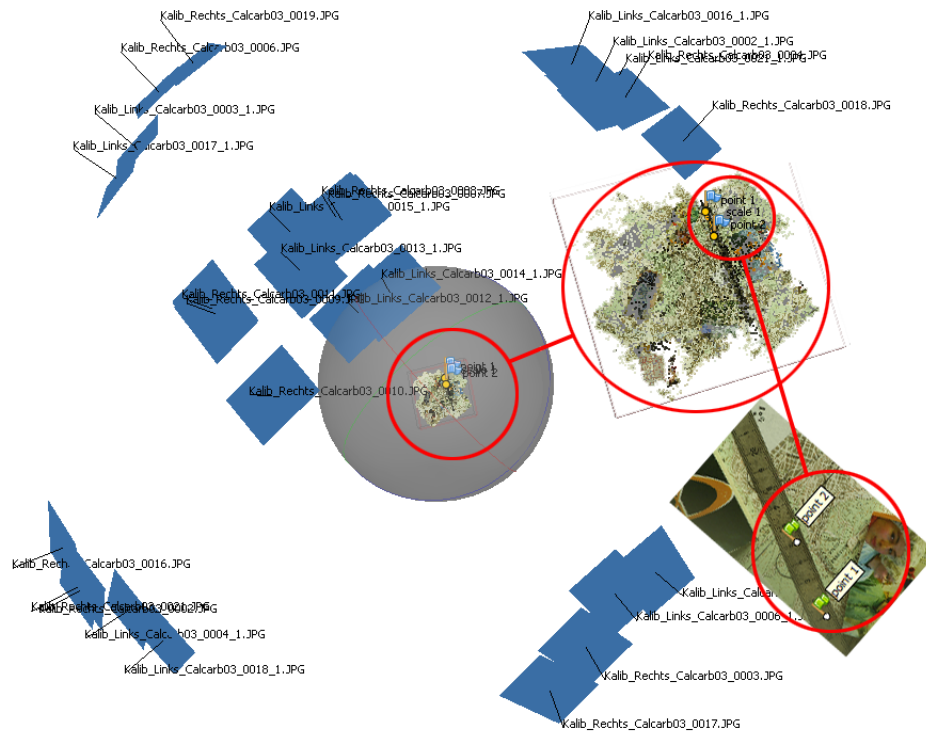


Figure 5: Three dimensional point map with camera positions and scale.

The analysis of this acquired data set is based on the software SURE, which is a computer code developed by the Institute of Photogrammetry at the University of Stuttgart.²⁵ The program calculates a point cloud using dense matching algorithms based on the epipolar geometry from the calibration. The wind tunnel testing images are cropped to the region of interest and the parameters in the orientation file are changed to the new image dimensions and the adapted coordinates of the principal point.

The orientation files calculated with PHOTOSCAN are used in SURE for the plasma wind tunnel image analysis. In a first step SURE rectifies the loaded image pair, then corresponding points in the two images are identified and calculated. During analysis, depth information of the points is dynamically used and compared along epipolar lines (Fig. 6). Due to the calibration, the camera positions with respect to each other are known. Therefore, a certain point of the object seen on the camera image in one camera lies on the epipolar line on the image of the other camera. The epipolar line is not necessarily a straight line nor is it horizontal in the images. Features in one image can be found on the line in the other image so that the algorithm can reconstruct the object's three-dimensional form. Within this work,

the geometrical distortions have been corrected in PHOTOSCAN. Then the epipolar lines are horizontal lines on one pixel line, simplifying the further analysis.

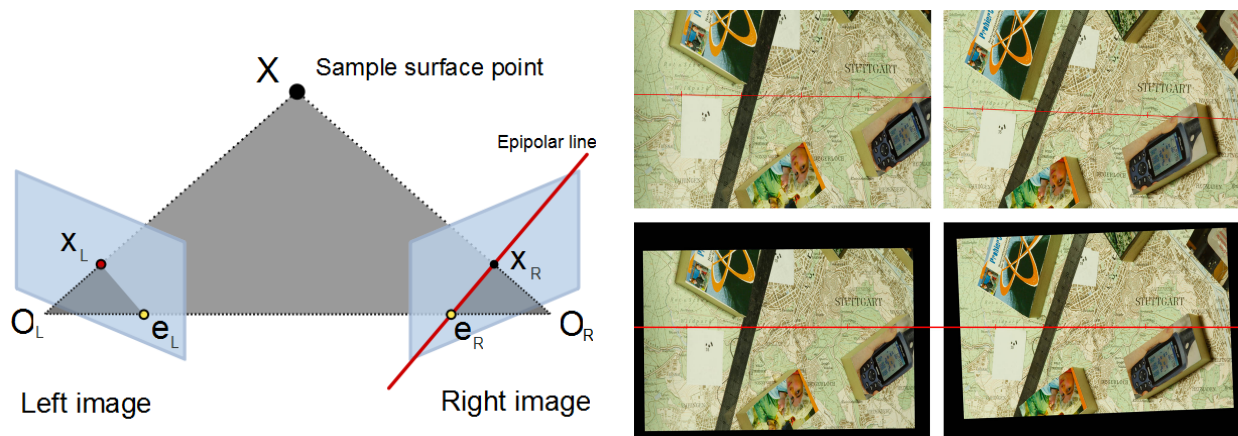


Figure 6: Definition of the epipolar line (left) and sample epipolar lines in calibration image pairs (right).

The result from this calculation step is a 3D-point cloud of the sample surface. The procedure is repeated for every image pair resulting in 90 three-dimensional probe surface point clouds. These clouds are then loaded in CLOUDCOMPARE, an open source software project for visualization. The edges of the probe usually can only be seen by one camera leading to calculation artefacts. Therefore, these parts are cut off. Afterwards, meshes are generated with the Delaunay Triangulation for each point cloud. Each mesh is a surface topography at a distinct time. With this information, distances between meshes, temporal evolution of certain probe surface features and local surface recession are analysed.

IV. Results

Fig. 7 shows an image of the probe during testing in the hot plasma flow. The bright plasma emission in the optical wavelength range is reduced by the cameras through the short exposure time (1/4000 s) and the additional ND filter. During start-up of the plasma generator, the sample is positioned outside the plasma jet. When the conditions are set, the sample is moved into the flow to the defined position. As mentioned, the left and the right camera are simultaneously acquiring images during test. The start time for the following analysis ($t = 0$ s) is set to the moment when the sample has reached the position on the center axis of the flow and is seen by both cameras at the calibrated location. For the measurements in this study a frame rate of 3 fps was chosen. During the plasma wind tunnel experiment, the cameras automatically acquire images. For a typical 30 s test, there is a total of 90 image pairs. Every image pair corresponds to a particular time during the testing. It is a trade-off between camera performance, data acquisition and data handling for the photogrammetry.

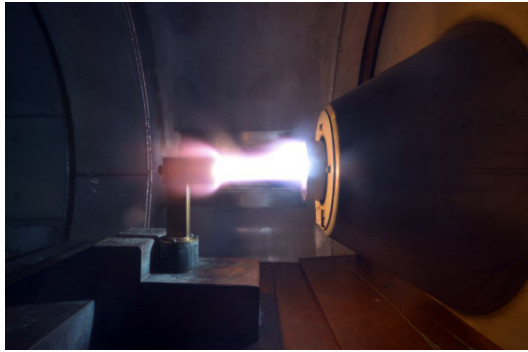


Figure 7: Side view of probe during experiment.

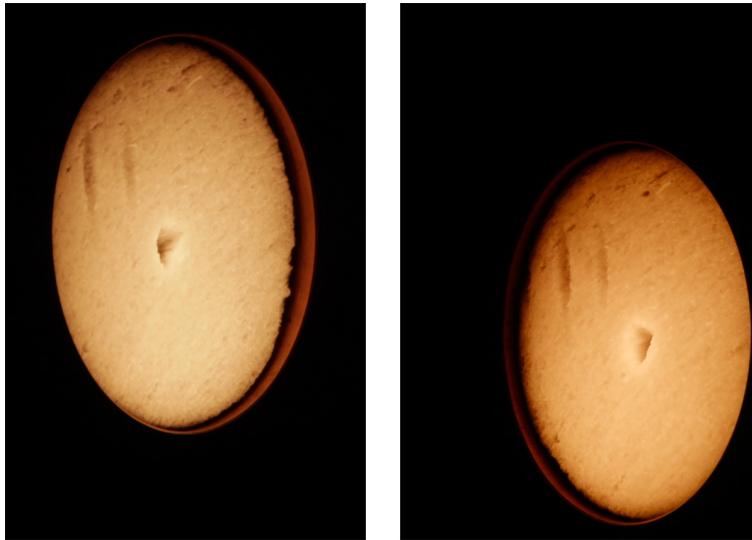


Figure 8: An example pair of the cropped images (left and right camera becomes left and right image, respectively).

As an example, Fig. 8 shows the cropped photographs taken at one instant in time at the beginning of the testing when the probe was in position. The darker spot in the center of the sample is a bore used for spectroscopic measurements which were ongoing in parallel.^{26,27} The two straight darker lines in the upper left corner of the sample were identified as indentations in the surface. In total, 96 image pairs were acquired. The dimensions of the cropped photos was $1049 \times 1562 \text{ px}^2$. In the following analysis, different image pairs are compared in order to derive surface recession and the corresponding recession rates.

In Fig. 9, exemplarily, eight different surface reconstructions at different instants of time during testing are shown. The surface is measured with 25000 px/cm^2 , corresponding to about 400 dpi. The plots show the surface where the gray scale is the depth in mm from the state of the beginning of the test ($t = 0 \text{ s}$) until the time of acquisition. So, the last image ($t = 32 \text{ s}$) shows the recession after 32 s. The present investigation allows, for the first time, conclusions to be drawn about behavior of the material surface during testing.

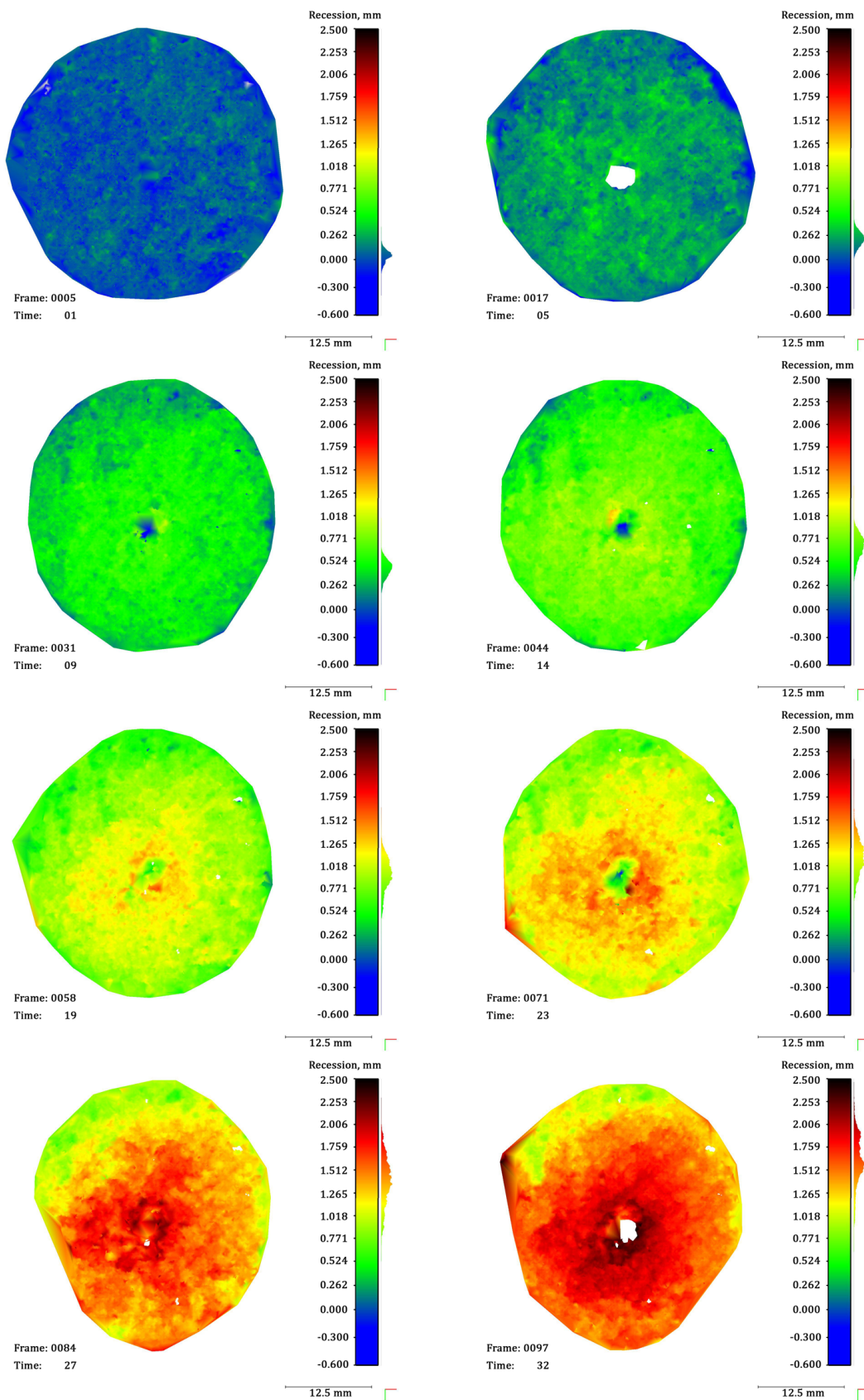


Figure 9: Exemplary sample surface structure during testing as derived from photogrammetry.

It can be seen that at the beginning the sample surface is quite a flat, slightly roughened surface. During the test, the surface is recessing (larger parts of the surface become darker) and the surface roughness increases. On the right side of each shown frame is a scale with the histogram of the depth distribution with respect to the first frame ($t = 0$ s). Thus, the peak here is the recession amount of the bulk of the material. The sample surface reconstruction using the photogrammetric setup is limited at the outer edge of the sample. During the testing, the sample's recession leads to areas that are no longer seen by one of the cameras, because the sample is offset to the copper ring. Therefore, in the first image, when the sample is flush mounted to the cooled copper holder (see Fig. 1), the whole sample surface is observable by both cameras and the resulting surface reconstruction is almost circular. With increasing test time, the sample boundaries become hidden behind the copper and a surface reconstruction is impossible. Therefore, the sample in the last image does not show a circular outer boundary.

The region around the centered bore hole recesses more than the outer region of the sample. Surface inhomogeneities, such as the two straight lines seen in the photo of Fig. 8, are seen as well because here the material changes differently from its surrounding regions. The recession rate is calculated from the position of all points in the reconstructed point cloud. Fig. 10 shows a histogram of the axial deviation in the recessing direction of the points of frame 19 ($t = 5$ s) and the points of frame 27 ($t = 8$ s) normalized to 1 s. For each point of the cloud, its recession is plotted in the histogram. On the abscissa the recession is marked in $\mu\text{m/s}$ and on the ordinate the quantity of points with the according value are plotted. The histogram is almost a gaussian distribution (solid line). Its maximum marks the arithmetic mean. The mode, representing the statistical maximum cumulation of a value is not always the same. In the figure, the standard deviation of the Gaussian distribution ($1\sigma, 2\sigma$) is plotted for completion. From this plot, it can be concluded that the mean surface recession rate between $t = 5$ s and $t = 8$ s is $50 \mu\text{m/s}$. The recession rate has been calculated for the whole test time, the result of which is plotted in Fig. 11.

Occasionally, and only for short times, a local increase of thickness was observed. The reason for this could be the fibre separation from the material before it is released. As the left side of the histogram in Fig. 10 is declined slightly steeper than the Gaussian distribution the arithmetic mean is shifted to a higher value. Comparing 85 histograms during the test results in the values as shown in Tab. 4. Although the results are very close, the mode value, as a solely statistical value, is more meaningful.

A comparison of mode, mean and median values during the test duration is shown in Fig. 11. In the lower section, the mass recession rate, in the upper section the recession is plotted. For the mass recession rate, always 9 frames (3 s) have been used to calculate the rate, normalised to one second. Therefore, the mass recession rate values start after 3 s.

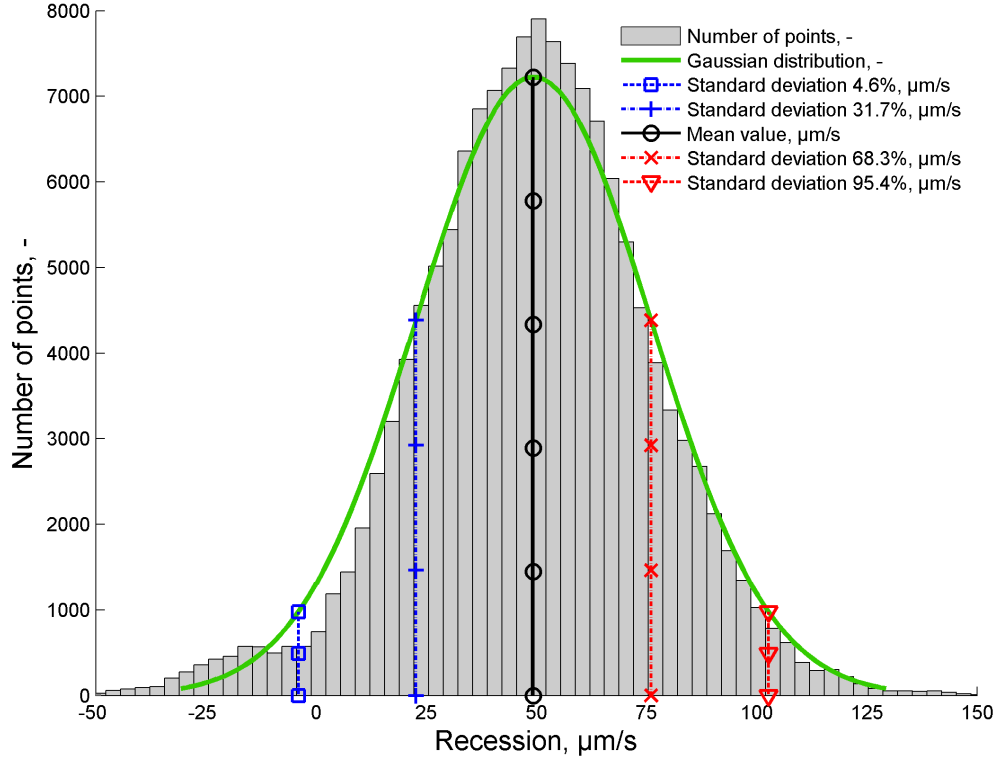


Figure 10: Histogram of the recession rate calculated from 3 seconds (9 image pairs) and normalised to recession rate per second.

Table 4: Comparison mean and mode values.

	Arithmetic mean, $\frac{\mu\text{m}}{\text{s}}$	Mode value, $\frac{\mu\text{m}}{\text{s}}$
Minima	33.3371	27.1253
Mean	52.4908	51.1780
Maxima	86.0236	75.9283

From this presentation it can be concluded that the recession rate is very constant over time. Since the sample was a porous carbon preform, an influence of a phenolic matrix as used in modern lightweight ablators was not investigated here. In Fig. 12 the recession rate during the test time is plotted together with the measured surface temperature. The surface temperature reaches a plateau of 2925 ± 30 K after a heating phase of about 10 s. From the photogrammetric analysis, an increase in recession rate from 4 s to 7 s could be interpreted. However, a linear fit gives

$$y_{rec}(t) = 0.0315t + 52.4349 \mu\text{m/s}. \quad (3)$$

This rate is very constant, i.e. the recession rate dependence from the surface temperature is weak. The mean recession rate of the sample is measured to $52.5 \mu\text{m/s}$.

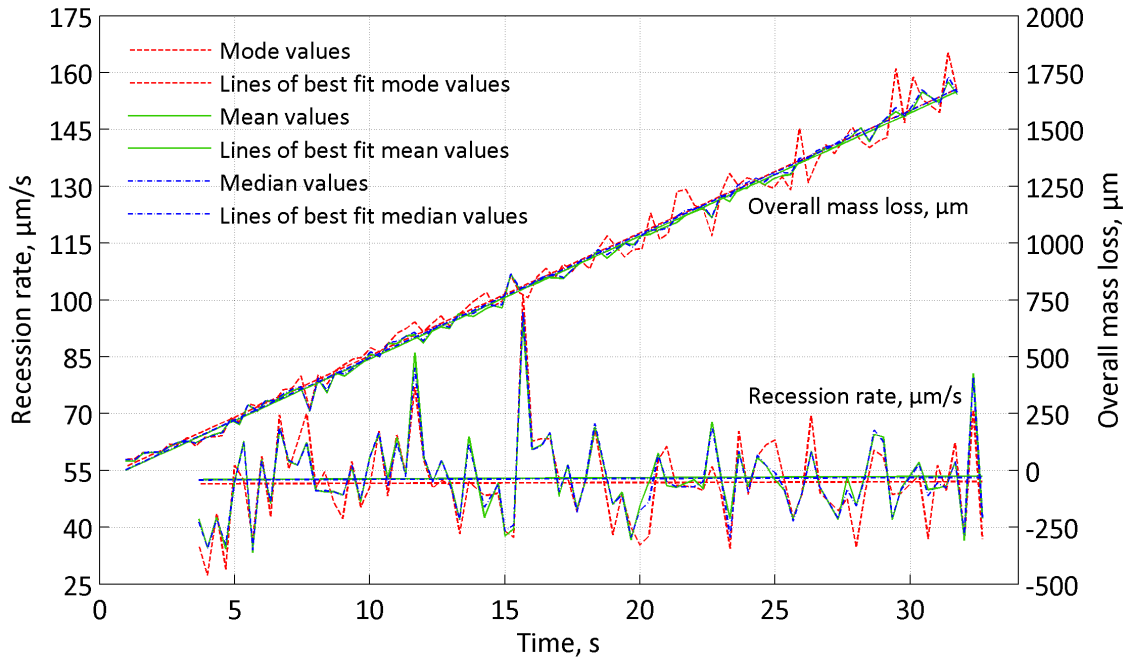


Figure 11: Recession rate and mass loss.

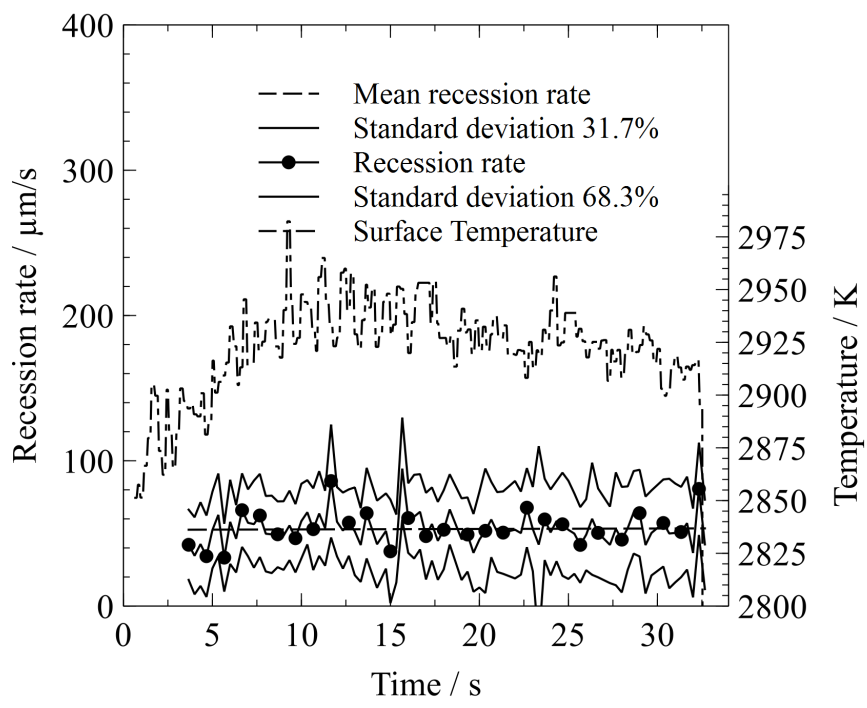


Figure 12: Recession rate and surface temperature over time.

The standard deviation, however, increases significantly (about 17 times higher than the mean value of the recession rate) and is plotted in Fig. 13,

$$y_{sigma}(t) = 0.5407t + 48.5602 \mu\text{m}/\text{s}. \quad (4)$$

In Fig. 8, there is a lighter circle around the darker bore hole, which is possibly a region of higher temperature and thus higher mass loss. At sharp corners, heat loads are higher resulting in more material loss as it can be seen in Fig. 14.

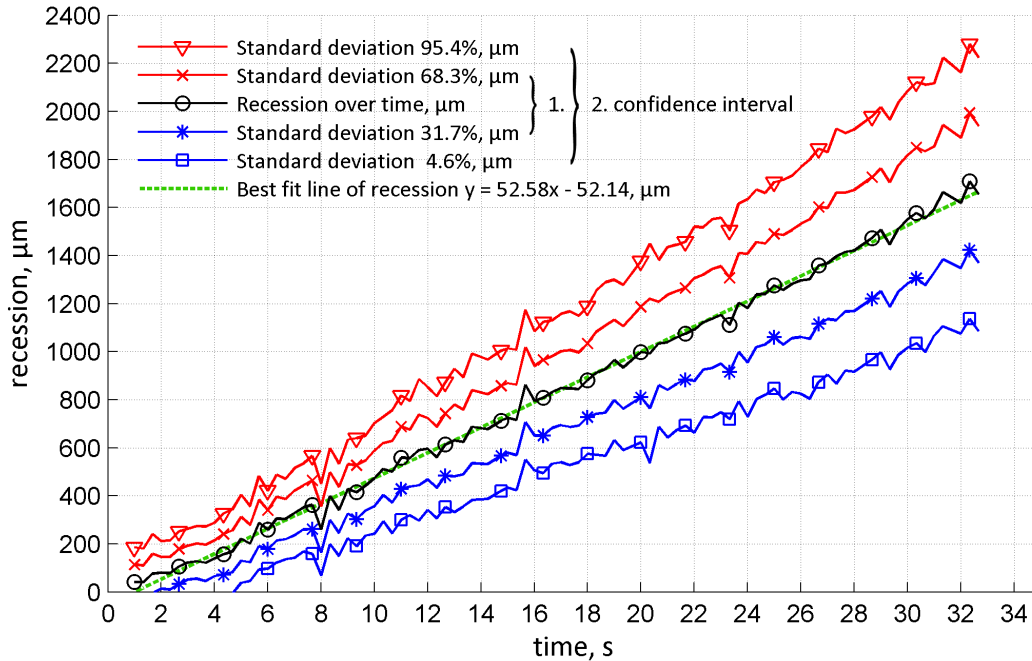


Figure 13: Recession over time with confidence interval ($1\sigma, 2\sigma$).

Fig 14 shows the last measured frame at $t = 32\text{ s}$ and Fig. 15 a side view of the photogrammetric result. Here, data in the recessing direction is amplified by a factor of 10 for better visualisation. The overall recession between the first analysed frame (frame 4, $t = 0\text{ s}$) and the last frame (frame 99, $t = 32\text{ s}$) is between $1300\ \mu\text{m}$ in the outer circle and $2100\ \mu\text{m}$ in the sample centre. As the mean mass recession rate is $52.5\ \mu\text{m}/\text{s}$ the overall mass loss results to $1700\ \mu\text{m}$. The sample thickness has also been manually measured before and after testing. Despite its high uncertainty, these measured values agree well with the photogrammetry. The inhomogeneity of the recession over the probe surface can have different reasons. Firstly, the material is not isotropic, secondly, the material holder induces cold outer parts of the probe leading to less material loss, and thirdly, the plasma flow does not homogeneously cover the surface. The samples haven't been equipped with in-depth sensors. Therefore, at this stage, a final conclusion for the higher centre recession can not be given.

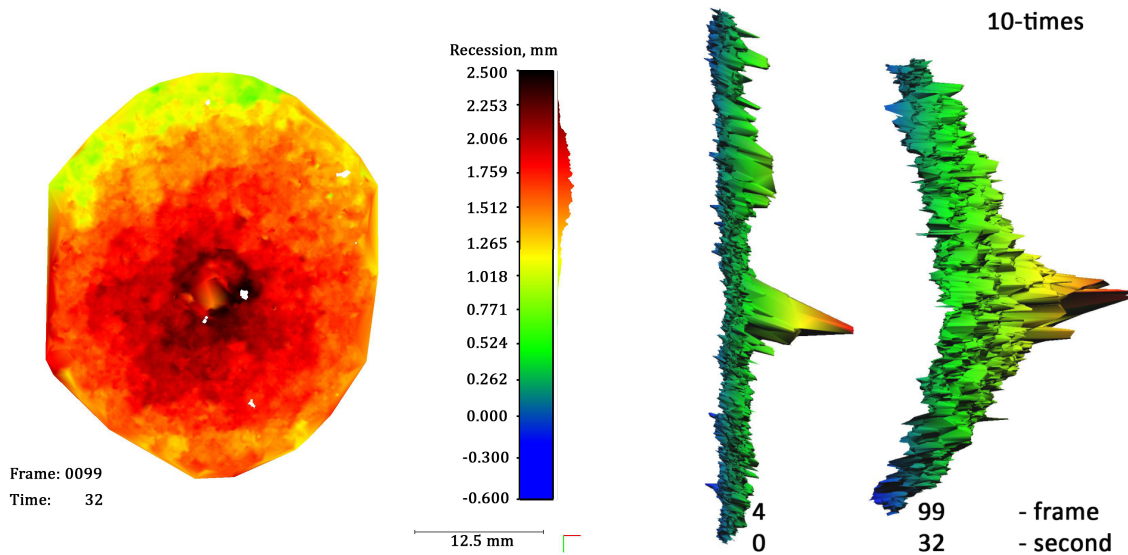


Figure 14: Surface structure at the end of the test ($t = 32$ s).

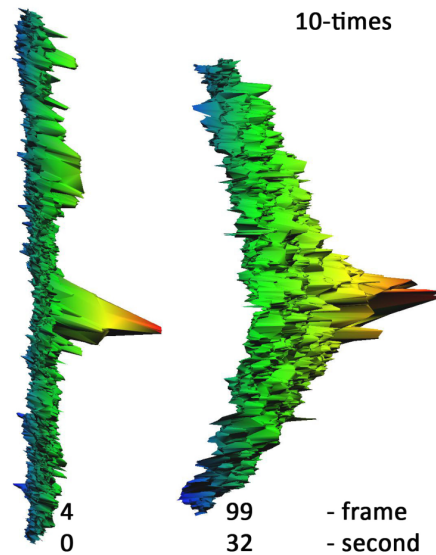


Figure 15: Side view of surface structure at beginning ($t = 0$ s, left) and end of test ($t = 32$ s, right).

Furthermore, the surface roughness increases throughout the test. It is assumed that this is due to the oxidation of the carbon fibres leading to higher porosity and thus higher surface roughness. Another indicator for this is the anomaly of the two straight lines in Fig. 8 which are also seen, for example in frame 4. There is less recession at these locations, leading to the conclusion that these features are indentations, i.e. material has been pressed here and thus the oxidation of the carbon is hindered. Their depth as measured from the photogrammetry is ≈ 0.3 mm.

V. Conclusion

The stereoscopic photogrammetric analysis of the surface recession in a high enthalpy air plasma flow allows a very detailed analysis of the ablation process. An optical resolution of 25000 points/cm² and a temporal resolution of up to three frames per second was achieved. The software used is well suited for this application with reasonable calculation complexity and acceptable computation time. The analysis of an experiment takes about one day. The surface resolution is very high, particularly compared to other methods used hitherto.

VI. Acknowledgement

The authors gratefully acknowledge the financial support by ESA through the research grant No. 2011/ITT-6632/PL. The support of the workshops at the German Research Center

and at IRS was very important and is gratefully acknowledged. We thank the colleagues from the group *Diagnostics for High-Enthalpy Flows* for the continuous and prompt help.

References

¹Lu, F. K. and Marren, D. E., editors, *Advanced Hypersonic Test Facilities*, Vol. 198 of *Progress in Astronautics and Aeronautics*, AIAA, 2002, ISBN 1-56347-541-3.

²Auweter-Kurtz, M. and Wegmann, T., “Overview of IRS Plasma Wind Tunnel Facilities,” *RTO Educational Notes*, Vol. 8, Oct. 1999.

³Chen, Y.-K. and Milos, F. S., “Ablation and Thermal Response Program for Spacecraft Heatshield Analysis,” *Journal of Spacecrafts and Rockets*, Vol. 36, No. 3, 1999.

⁴Löhle, S., Eichhorn, C., Steinbeck, A., Lein, S., Herdrich, G., Röser, H.-P., and Auweter-Kurtz, M., “Oxygen Plasma Flow Properties deduced from Laser-induced Fluorescence and Probe Measurements,” *Applied Optics*, Vol. 47, No. 13, 2008, pp. 1837–1845.

⁵Lachaud, J., Cozmuta, I., and Mansou, N. N., “Multiscale Approach to Ablation Modeling of Phenolic Impregnated Carbon Ablators,” *Journal of Spacecrafts and Rockets*, Vol. 47, No. 6, 2010.

⁶Beerman, A. F., Lewis, M. J., Starkey, R. P., and Cybyk, B. Z., “Significance of Nonequilibrium Surface Interactions in Stardust Return Capsule Ablation Modeling,” *Journal of Thermophysics and Heat Transfer*, Vol. 23, No. 3, 2009.

⁷Eswein, N., Herdrich, G., Fasoulas, S., and Röser, H.-P., “Investigation of Graphite Ablation at IRS,” *42nd Thermophysics Conference*, AIAA, 2011.

⁸Santos, J. A., Oishi, T., and Martinez, E. R., “Isotherm Sensor Calibration Program for Mars Science Laboratory Heat Shield Flight Data Analysis,” *42nd AIAA Thermophysics Conference*, No. AIAA 2011-3955, AIAA, 2011.

⁹White, T., Cozmuta, I., Santos, J. A., Laub, B., and Mahzari, M., “Proposed Analysis Process for Mars Science Laboratory Heat Shield Sensor Plug Flight Data,” *42nd AIAA Thermophysics Conference*, No. AIAA 2011-3957, AIAA, 2011.

¹⁰Sherrouse, P. and Carver, D., “Demonstrated Real-Time Recession Measurements of Flat Materials During Testing in High-Enthalpy Flows,” *30th Aerospace Science Meeting and Exhibit*, AIAA, 1992.

¹¹Schairer, E. T. and Heineck, J. T., “Photogrammetric Recession Measurements of Ablative Materials in Arcjets,” *Measurement Science and Technology*, Vol. 21, 2010.

¹²Auweter-Kurtz, M. and Wegmann, T., “Overview of IRS Plasma Wind Tunnel Facilities,” *RTO AVT/VKI Special Course on Measurement Techniques for High Enthalpy Plasma Flows*, No. AC/323(AVT)TP/23 in RTO-EN-8, 2000.

¹³Wernitz, R., Eichhorn, C., Herdrich, G., Löhle, S., Fasoulas, S., and Röser, H.-P., “Plasma Wind Tunnel Investigation of European Ablators in Air Using Emission Spectroscopy,” *42nd AIAA Thermophysics Conference*, 2011.

¹⁴Helber, B., Chazot, O., Magin, T., and Hubin, A., “Ablation of carbon preform in the VKI Plasma-tron,” *43rd Thermophysics Conference*, No. AIAA 2012-2876, AIAA, 2012.

¹⁵Loehle, S. and Jenniskens, P., “High Resolution Spectroscopy of the Hayabusa Re-entry using a Fabry-Perot Interferometer,” *Journal of Spacecrafts and Rockets*, 2014, in press.

¹⁶Löhle, S., Brandis, A., Hermann, T., and Peter, J., “Numerical Investigation of the Re-entry Flight of Hayabusa and Comparison to Flight and Ground Testing Data,” *43rd AIAA Thermophysics Conference*, AIAA, LA, 2012.

¹⁷Leyland, P., McIntyre, T., Sheikh, U., Eichman, T., Zander, F., Morgan, R., Löhle, S., Hermann, T., De Filipis, F., Trifoni, E., and Cillo, G., “VUV Radiation Measurements for Ablation-Radiation Coupling,” *ESA Radiation of High Temperature Gases Workshop*, ESA, 2012.

¹⁸Zoby, E. V., “Empirical Stagnation-Point Heat-Transfer Relation in Several Gas Mixtures at High Enthalpy Levels,” *NASA Technical Note*, , No. TN D-4799, 1968.

¹⁹Fay, J. A. and Riddell, F. R., “Theory of Stagnation Point Heat Transfer in Dissociated Air,” *AIAA Journal*, Vol. Volume 25, No. 2, 1958, pp. 373–386.

²⁰Marr, J., *Untersuchung von photogrammetrischen Methoden zu in-situ Oberflächenanalyse von Ablatoren*, Diplomarbeit, Universität Stuttgart, 2011, IRS-11-S18.

²¹Pitzer, P., *Einfluss refraktiver und reflektiver Elemente auf die photogrammetrische Kamerakalibrierung*, Bachelorarbeit, Universität Stuttgart, 2012.

²²“Agisoft Photoscan,” online, May 2014, www.agisoft.ru.

²³Wester-Ebbinghaus, W., *Verfahren zur Feldkalibrierung von photogrammetrischen Aufnahmekammern im Nahbereich*, No. 275, DGK Reihe B, 1985.

²⁴Luhmann, T., *Nahbereichsphotogrammetrie: Grundlagen, Methoden und Anwendungen*, Wichmann, Berlin, 3rd ed., 2010.

²⁵Rothermel, M., Wenzel, K., Fritsch, D., and Haala, N., “SURE: Photogrammetric Surface Reconstruction from Imagery,” Berlin, Dec. 2012.

²⁶Hermann, T., Zander, F., Fulge, H., Löhle, S., and Fasoulas, S., “Experimental Setup for Vacuum Ultraviolet Spectroscopy for Earth Re-entry Testing,” *30th Aerodynamic Measurement Technology and Ground Testing Conference*, AIAA, 2014, submitted.

²⁷Löhle, S., Hermann, T., Zander, F., Fulge, H., and Marynowski, T., “Ablation Radiation Coupling Investigation in Earth Re-entry Using Plasma Wind Tunnel Experiments,” *30th Aerodynamic Measurement Technology and Ground Testing Conference*, AIAA, 2014, submitted.